Electron-impact excitation of the $(5d^{10}6s)^2S_{1/2} \rightarrow (5d^{10}6p)^2P_{1/2,3/2}$ resonance transitions in gold atoms

M. Maslov,[1] M. J. Brunger,[1] P. J. O. Teubner,[1] O. Zatsarinny,[2] K. Bartschat,[2] D. Fursa,[3] I. Bray,[3] and R. P. McEachran[4]
[1]*ARC Centre for Antimatter-Matter Studies and School of Chemistry, Physics and Earth Sciences, Flinders University, G.P.O. Box 2100, Adelaide 5001, Australia*
[2]*Department of Physics and Astronomy, Drake University, Des Moines, Iowa 50311, USA*
[3]*ARC Centre for Antimatter-Matter Studies and Department of Imaging and Applied Physics, Curtin University, Perth, Western Australia 6845, Australia*
[4]*ARC Centre for Antimatter-Matter Studies and Research School of Physical Sciences and Engineering, Australian National University, Canberra, Australian Capital Territory 0200, Australia*
(Received 10 April 2008; published 19 June 2008)

Results from a joint experimental and theoretical investigation of electron-impact excitation of the $(5d^{10}6s)^2S_{1/2} \rightarrow (5d^{10}6p)^2P_{1/2,3/2}$ resonance transitions in gold atoms are presented. The calculations were performed using three fully relativistic approaches, namely, a distorted-wave ansatz, a convergent close-coupling method, and a *B*-spline *R*-matrix method. The experimental data are independently normalized to the Bethe-Born formula using the currently preferred experimental values of the optical oscillator strengths. There is generally good agreement between the measured and predicted energy dependences of the integral cross section, provided that sufficient care is taken in the theoretical structure models to ensure that the proper optical oscillator strengths for the two transitions are obtained. A strong resonance feature seen only in the near-threshold excitation of the $(5d^{10}6p)^2P_{1/2}$ state is classified as a $(5d^{10}6p^2)^1D_2$ temporary state of the negative gold ion.

DOI: 10.1103/PhysRevA.77.062711 PACS number(s): 34.80.Dp

I. INTRODUCTION

Electron-atom collisions lie at the heart of many physical phenomena, so that there is always a demand for data in collision cross sections in such fields as atmospheric physics, astrophysics, and plasma physics. In particular, in astrophysics, resonant lines due to the $(5d^{10}6p)^2P_{1/2,3/2}$ gold doublet are observed in the spectra of Hg-Mn stars, so that data on the excitation mechanism for this doublet are needed in the study of the atmospheres of those stars [1]. From an applied perspective, the most relevant application is in the further development of the gold vapor laser (GVL), which generates one red (627.8 nm) and one ultraviolet (312.3 nm) line of high spatial quality. While GVLs have been extensively commercialized, new types and new designs continue to be investigated particularly for use in laser therapy in medicine [2]. At this point we note, however, that little industrial work has been undertaken in understanding at the nanoscale level how this laser actually functions. While it is understood that the $(5d^{10}6p)^2P_{1/2}$ and $(5d^96s^2)D_{3/2}$ states of gold serve as the upper and lower working levels, respectively, in the excitation scheme of the 627.8 nm GVL line, and that the $(5d^{10}6p)^2P_{1/2}$ state serves as the upper level in the excitation scheme of the 312.3 nm GVL line, no quantitative explanation for the population inversion process exists. As the $(5d^{10}6p)^2P_{1/2,3/2}$ and $(5d^96s^2)D_{3/2}$ levels are populated in the GVL by electron impact due to an electric discharge during operation, the achievement of the population inversion in the GVL critically depends on their absolute excitation cross sections. Unfortunately, such absolute cross sections, prior to this study, were limited to an early relativistic distorted-wave calculation by Zeman *et al.* [3] and some differential cross sections from Holst *et al.* [4]. Note that neither of those works extended to the threshold energy region. Hence, one of the aims of the present study was to provide reliable absolute integral cross sections, over a range from threshold to ~600 eV, so that quantitative modeling of the GVL might ultimately be undertaken. As gold is quite heavy ($Z=79$), another aim of the present joint experimental and theoretical study was to probe the importance of relativistic effects on the collision process.

A brief description of the experimental setup is given below, followed by a summary of the numerical methods. The results are presented and discussed in Sec. IV, and finally some conclusions are drawn.

II. EXPERIMENTAL DETAILS

Excitation functions for the $(5d^{10}6p)^2P_{1/2}$ and $(5d^{10}6p)^2P_{3/2}$ states were measured by observing photons emitted from the interaction region with a photomultiplier tube equipped with an appropriate interference filter for each line. The interaction region (see Fig. 1 for a schematic diagram) was defined by the intersection of a focused electron beam with a beam of gold atoms. The electron beam was formed in a standard electrostatically focused electron gun that produced beam currents of between 0.5 and 5 μA over the energy range of the experiments. An oxide cathode was used as a source of electrons, and hence the energy spread in the beam was only about 0.3 eV. Since oxide cathodes are subject to a significant contact potential, it was necessary to calibrate the beam energy regularly. This was achieved by analyzing the threshold behavior of the excitation function over a range of about 1 V near threshold. This procedure not only enabled an accurate determination of the contact poten-

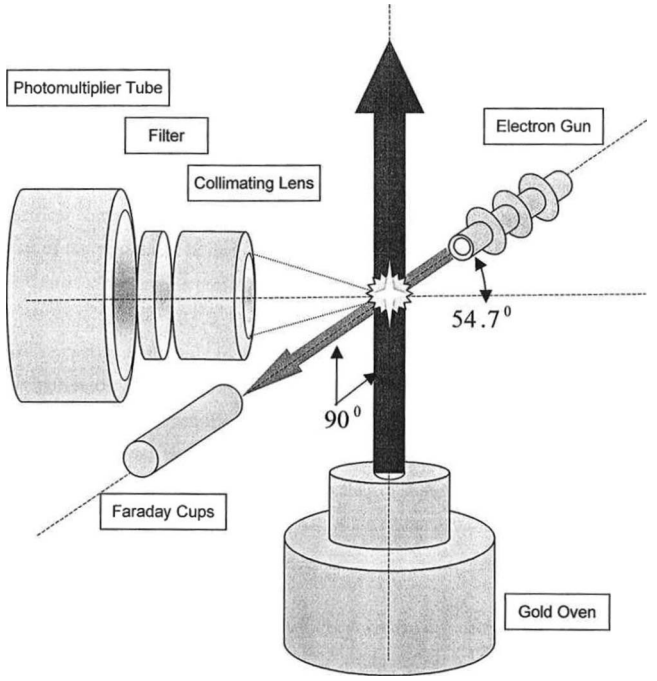

FIG. 1. Schematic diagram showing the directions of the gold beam, the electrons, and the detected photon emission. Note that the photomultiplier tube is positioned at the "magic angle" to avoid polarization effects in the emitted radiation.

tial, but also allowed us to confirm that the present energy spread was typical for an oxide cathode.

The gold atoms were produced by heating gold wire in a molybdenum crucible, which was heated to temperatures up to 1600 K by electron bombardment. Great care was taken to isolate the gold beam from these electrons. At this temperature the number density of gold atoms in the interaction region was about 4×10^{14} m^{-3}. The diameter of the gold beam was 7.5 mm and its angular divergence was 0.12 rad [full width at half maximum (FWHM)]. The oven temperature was measured with a thermocouple and the temperature was stabilized to 1 K over the course of the run by a feedback loop that controlled the electron emission as the oven temperature varied.

The oven assembly was thermally insulated from the vacuum chamber and the supports were water cooled. Nevertheless the ambient temperature of the photomultiplier mount could rise substantially over the course of a run. This caused the dark count rate in the photomultiplier tube to increase significantly. Consequently, each run was limited to less than 2 h and the electron beam was chopped at 1 Hz. We estimate that the temperature dependence of the transmittance of the interference filters contributed errors of $\pm1.5\%$ and $\pm2\%$ in the values of the $(5d^{10}6p)^2P_{1/2}$ and $(5d^{10}6p)^2P_{3/2}$ excitation functions, respectively. The difference arises from the different transmission characteristics of the two filters.

The output from the photomultiplier tube was amplified and counted in one of two scalers that were gated in synchronism with the electron beam. Note that the photomultiplier tube was positioned at the so-called magic angle in order to avoid polarization effects from the emitted radiation.

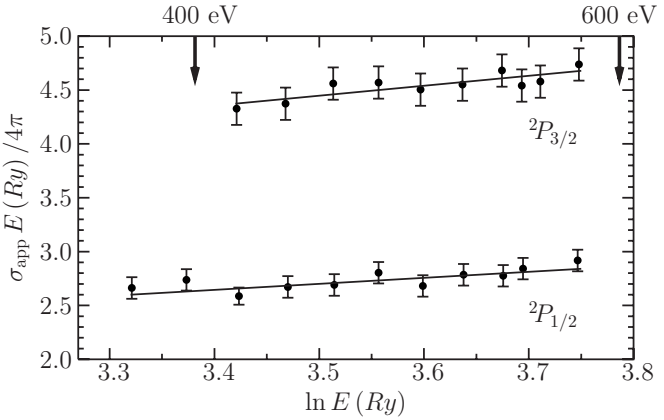

FIG. 2. Bethe-Born plots of the experimental data for electron-impact excitation of the $(5d^{10}6p)^2P_{1/2}$ and $(5d^{10}6p)^2P_{3/2}$ states in gold. The slopes of the lines from the least-squares fits enabled us to establish the absolute cross-section scales in each case (see text).

The excitation functions contain cascade contributions from higher excited states. At incident energies in excess of about 200 eV, however, these contributions should be small, because the cascades will be from S and D states, whose direct excitations from the ground state are optically forbidden. It is well known that the cross sections for exciting these states are much smaller than those for the resonant P states.

Denoting by $\mathcal{S}$ the observed photon count rate, Fig. 2 reveals an essentially linear relationship between the product $\mathcal{S}E$ and ln E for both states at incident electron energies (E) between ~400 and 600 eV. The Bethe-Born approximation predicts (in atomic units) [5] that

$$QE = \frac{4\pi f_o}{E_{exc}} \ln E, \tag{1}$$

where f_o is the optical oscillator strength and E_{exc} is the excitation energy of the respective state. In the present case $f_o=0.176\pm0.003$ for the $(5d^{10}6p)^2P_{1/2}$ state and $f_o=0.351\pm0.015$ for the $(5d^{10}6p)^2P_{3/2}$ state [6].

Using these oscillator strengths and the slopes from the Bethe-Born plots in each case, we were able to normalize our cross sections at these high energies. These normalizations, in turn, fixed the absolute values over the entire energy range. We also note that the Bethe-Born approximation predicts that the cross sections for excitation of the S and D states will fall off as $1/E^2$ at high energies. Consequently, it is not surprising that our excitation functions appear to be nearly free of cascades in the energy range used for the normalization. Nevertheless, the normalizing procedure introduces the most significant source of uncertainty in the experiments. We estimate it to be overall $\pm20\%$. The present experimental integral cross sections for the $(5d^{10}6p)^2P_{1/2}$ and $(5d^{10}6p)^2P_{3/2}$ levels are respectively listed in Tables I and II.

III. COMPUTATIONAL DETAILS

The numerical calculations for this work are based upon fully relativistic distorted-wave (RDW), convergent close-

TABLE I. Present experimental integral cross sections (a_0^2) for electron impact excitation of the $(5d^{10}6p)^2P_{1/2}$ state in gold. The estimated uncertainty on these data is $\sim \pm 20\%$.

E (eV)	σ (a_0^2)	E (eV)	σ (a_0^2)	E (eV)	σ (a_0^2)	E (eV)	σ (a_0^2)	E (eV)	σ (a_0^2)	E (eV)	σ (a_0^2)	E (eV)	σ (a_0^2)
4.28	0.20	5.38	4.99	7.14	6.61	8.94	6.38	11.53	6.75	15.44	6.29	73.90	3.36
4.30	0.25	5.43	4.86	7.23	6.61	8.99	6.27	11.63	6.64	15.73	6.31	77.90	3.26
4.33	0.25	5.48	4.86	7.28	6.64	9.04	6.42	11.73	6.57	16.02	6.28	81.91	3.18
4.35	0.43	5.52	4.75	7.33	6.59	9.09	6.42	11.82	6.53	16.32	6.33	85.91	3.07
4.38	0.55	5.57	4.90	7.38	6.59	9.14	6.45	11.92	6.59	16.61	6.52	89.92	3.11
4.40	0.62	5.62	4.79	7.43	6.61	9.19	6.33	12.02	6.41	16.90	6.29	93.92	2.89
4.42	0.81	5.67	5.03	7.48	6.45	9.24	6.49	12.12	6.28	17.20	6.54	96.83	2.86
4.45	1.08	5.72	5.06	7.53	6.31	9.28	6.53	12.22	6.44	17.49	6.38	107	2.71
4.47	1.26	5.77	5.14	7.58	6.35	9.33	6.44	12.31	6.38	17.78	6.37	117	2.59
4.50	1.66	5.82	5.16	7.62	6.26	9.38	6.52	12.41	6.43	18.08	6.35	127	2.42
4.52	1.95	5.87	5.42	7.67	6.32	9.43	6.37	12.51	6.33	18.37	6.25	137	2.32
4.55	2.42	5.91	5.43	7.72	6.26	9.48	6.46	12.61	6.42	18.66	6.17	147	2.19
4.57	2.92	5.96	5.43	7.77	6.22	9.53	6.56	12.70	6.45	18.96	6.35	157	2.08
4.60	3.27	6.01	5.44	7.82	6.14	9.58	6.43	12.80	6.41	19.25	6.17	177	1.96
4.62	3.81	6.06	5.43	7.87	6.13	9.63	6.46	12.90	6.43	19.54	6.17	197	1.87
4.64	4.41	6.11	5.55	7.92	6.10	9.68	6.43	13.00	6.43	19.83	6.07	217	1.73
4.67	4.87	6.16	5.54	7.97	6.09	9.72	6.52	13.09	6.54	20.84	6.05	237	1.61
4.69	5.38	6.21	5.37	8.01	6.17	9.77	6.40	13.19	6.35	21.84	6.00	257	1.55
4.72	5.74	6.26	5.41	8.06	6.12	9.82	6.47	13.29	6.39	22.84	5.89	277	1.49
4.74	5.87	6.31	5.54	8.11	6.19	9.87	6.50	13.39	6.34	23.84	5.83	297	1.41
4.77	6.30	6.35	5.60	8.16	6.19	9.97	6.48	13.48	6.35	24.84	5.83	317	1.40
4.79	6.49	6.40	5.47	8.21	6.39	10.07	6.44	13.58	6.39	25.84	5.75	337	1.35
4.82	6.60	6.45	5.48	8.26	6.22	10.16	6.36	13.68	6.27	26.84	5.66	357	1.30
4.84	6.41	6.50	5.46	8.31	6.34	10.26	6.37	13.78	6.39	27.84	5.52	377	1.21
4.86	6.59	6.55	5.59	8.36	6.35	10.36	6.44	13.88	6.28	28.85	5.61	397	1.18
4.89	6.24	6.60	5.64	8.41	6.22	10.46	6.53	13.97	6.34	29.85	5.52	417	1.06
4.91	6.34	6.65	5.54	8.45	6.24	10.55	6.40	14.07	6.34	33.85	5.29	437	1.05
4.94	6.04	6.70	5.74	8.50	6.27	10.65	6.39	14.17	6.23	37.86	5.03	457	1.01
4.99	5.93	6.75	5.95	8.55	6.42	10.75	6.42	14.27	6.35	41.86	4.71	477	1.00
5.04	5.88	6.79	6.00	8.60	6.27	10.85	6.43	14.36	6.33	45.86	4.58	497	0.92
5.08	5.97	6.84	6.13	8.65	6.39	10.95	6.63	14.46	6.36	49.87	4.37	517	0.92
5.13	5.91	6.89	6.23	8.70	6.33	11.04	6.68	14.56	6.38	53.88	4.28	537	0.88
5.18	5.97	6.94	6.51	8.75	6.31	11.14	6.52	14.66	6.19	57.88	4.02	547	0.89
5.23	5.73	6.99	6.37	8.80	6.37	11.24	6.50	14.75	6.32	61.89	3.82	577	0.86
5.28	5.38	7.04	6.56	8.85	6.30	11.34	6.62	14.85	6.27	65.89	3.63		
5.33	5.11	7.09	6.61	8.89	6.30	11.43	6.54	15.15	6.35	69.90	3.54		

coupling (RCCC), and Dirac B-spline R-matrix (DBSR) methods. As a perturbative approach, the RDW is expected to be reasonably accurate at intermediate to high collision energies, typically starting at about two to three times the ionization threshold (20–30 eV in this case). On the other hand, the RCCC and DBSR are general methods that are, in principle, applicable at all incident electron energies. The numerical implementation, however, limits the DBSR method to relatively low incident energies, where it is very efficient when results for a large number of energies are required, as is often the case for near-threshold resonance structures. Contrary to this, the RCCC approach can be used at all energies, but it is currently limited to treating the target as a quasi-one-electron system (see below).

An important aspect, especially for a relatively complex target such as gold, is the *structure description*, which is by no means trivial. In fact, it is well known that nonrelativistic approaches predict oscillator strengths for the $(5d^{10}6s)^2S_{1/2} \rightarrow (5d^{10}6p)^2P_{1/2,3/2}$ resonance transitions that are about a factor of 2 too large (see below). This is still the case even when multiconfiguration Dirac-Fock wave functions are employed, except if these configurations account properly for polarizability effects. Since such *ab initio* wave functions are very difficult to use in subsequent collision calculations, quick

TABLE II. Present experimental integral cross sections (a_0^2) for electron impact excitation of the $(5d^{10}6p)^2P_{3/2}$ state in gold. The estimated uncertainty on these data is $\sim \pm 20\%$.

E (eV)	σ (a_0^2)	E (eV)	σ (a_0^2)	E (eV)	σ (a_0^2)	E (eV)	σ (a_0^2)	E (eV)	σ (a_0^2)
4.65	0.27	6.31	7.52	7.99	8.52	16.30	8.65	177	3.29
4.70	0.50	6.41	7.81	8.09	8.08	17.30	8.27	197	3.10
4.75	0.60	6.51	7.66	8.17	8.11	18.30	8.40	217	2.90
4.80	0.67	6.60	7.73	8.28	7.99	19.30	8.41	237	2.74
4.85	1.13	6.70	7.73	8.31	8.09	20.30	8.24	257	2.57
4.90	1.62	6.80	7.81	8.51	8.25	21.30	8.14	277	2.45
4.94	2.32	6.90	7.87	8.66	8.41	22.30	7.97	297	2.37
4.99	3.15	7.00	8.19	8.91	8.22	23.30	7.93	317	2.30
5.04	4.27	7.09	8.40	9.11	8.41	26.30	7.65	337	2.16
5.09	5.33	7.11	8.67	9.14	8.65	31.30	7.48	357	1.99
5.14	6.31	7.16	8.89	9.31	8.36	36.30	7.01	377	1.94
5.19	6.75	7.19	8.92	9.81	8.76	41.30	6.95	397	1.83
5.24	7.35	7.21	8.97	10.14	8.85	46.30	6.43	417	1.77
5.29	7.41	7.25	8.95	10.31	8.60	51.30	6.25	437	1.71
5.33	7.47	7.30	9.40	10.81	8.66	56.30	6.04	457	1.71
5.38	7.38	7.35	9.47	11.15	8.67	61.30	5.81	477	1.64
5.43	7.09	7.40	9.12	11.31	8.60	66.30	5.45	497	1.55
5.53	6.98	7.45	9.47	11.81	8.68	71.30	5.40	517	1.51
5.58	6.74	7.50	8.91	12.31	8.60	76.30	5.18	537	1.49
5.63	6.92	7.55	8.84	12.81	8.80	81.30	5.09	547	1.42
5.72	6.73	7.60	8.79	13.30	8.74	86.30	5.00	557	1.41
5.82	6.91	7.65	8.63	13.80	8.67	91.30	4.80	577	1.41
5.92	7.21	7.68	8.43	14.30	8.73	96.30	4.67		
6.02	7.03	7.74	8.22	14.80	8.68	117	4.28		
6.12	7.42	7.79	8.20	15.30	8.70	137	3.89		
6.21	7.41	7.89	8.16	15.80	8.72	157	3.56		

fixes of this problem range from the use of semiempirical core potentials [7] to a simple rescaling of the results using the ratio of experimental and theoretical oscillator strengths [8]. Another difficulty in gold is the filled and very diffuse $5d$ subshell. While part of the Au spectrum consists of Rydberg-like ($\ldots 5d^{10}nl$) states, the first excited state has the dominant configuration $5d^9 6s^2$. Hence one can expect a significant configuration dependence of the $5d$ orbital.

In the sections below, we briefly summarize the most important aspects of the structure and the collision models applied in the RDW, RCCC, and DBSR calculations. Since all these collision methods have been or will be described in other publications, relevant references rather than detailed descriptions are given here.

A. RDW calculations

The RDW method for the excitation of alkali-metal and alkali-metal-like atoms was described in detail by Zeman *et al.* [9]. Consequently, we will only list the principal differences employed here for the excitation of the $(6p)^2P_{1/2}$ and the $(6\bar{p})^2P_{3/2}$ levels of gold.

The ground and excited states of gold were determined in two different models using a modified version of the multiconfiguration Dirac-Fock (MCDF) code of Grant *et al.* [10], which allows for the incorporation of core polarization potentials. In the first model, the core orbitals were determined in a fully varied Dirac-Fock procedure, and the core polarization potential $V_c(r)$ of Au^+ was subsequently generated by the polarized-orbital method. With the core orbitals held fixed, the $6s$, $6\bar{p}$, and $6p$ valence orbitals were then determined in a polarized frozen-core procedure, which included the above core polarization potential. Overall scaling factors of this core potential yielded the experimental ionization energies of 0.339 037, 0.168 821, and 0.151 433 a.u. of the $6s$, $6\bar{p}$, and $6p$ valence states. These scaling factors were 0.981 24, 1.076 47, and 1.206 48, respectively. In the second model, the valence orbitals were determined in a fully varied multiconfiguration Dirac-Fock procedure, which included the nine configurations $5\bar{d}^4 5d^6 6s$, $5\bar{d}^3 5d^6 6s^2$, $5\bar{d}^4 5d^5 6s^2$, $5\bar{d}^4 5d^6 6\bar{p}$, $5\bar{d}^4 5d^6 6p$, $5\bar{d}^4 5d^4 6\bar{p}^2 6s$, $5\bar{d}^4 5d^4 6p^2 6s$, $5\bar{d}^2 5d^6 6\bar{p}^2 6s$, and $5\bar{d}^2 5d^6 6p^2 6s$, respectively.

When the frozen-core approximation is used for the alkali-metal and alkali-metal-like atoms, Bersuker [11] and later Hameed *et al.* [12] showed that it is necessary to modify the dipole operator in order to obtain reliable oscillator strengths for these one-electron systems. This is par-

ticularly true for silver and gold. The asymptotic form of the modified dipole length operator is given by $r-\alpha_d/r^3$ where α_d is the dipole polarizability of the core. This modification incorporates the induced dipole moment of the core electrons. It is also required in most multiconfiguration calculations of these oscillator strengths [13–15]. In the latter calculations, it was also necessary to introduce some form of cutoff parameter in order to prevent the modified dipole operator from diverging at the origin. In the present work, we replaced the dipole length operator by $r+rU_c(r)$. Here $U_c(r)$ is the reduced core polarization potential, which behaves as $-\alpha/r^4$ at infinity. However, since $U_c(r)$ varies as r^2 near the origin, it is not necessary to introduce a cutoff parameter. In the frozen-core model, the oscillator strengths for the $6s_{1/2}\rightarrow 6p_{1/2}$ and $6s_{1/2}\rightarrow 6p_{3/2}$ transitions are 0.214 and 0.453, respectively, when the modified dipole operator is used. These values are approximately 20% and 30% too large and illustrate the importance of "relaxing" the diffuse $5\bar{d}$ and $5d$ orbitals in the determination of the valence orbitals. In the multiconfiguration model, the corresponding oscillator strengths are given by 0.163 and 0.364, respectively, in much better agreement with experiment.

In order to allow for the induced dipole moment of the core electrons, the corresponding modification of the interaction potential $V_{\rm int}(r)$ in the RDW method is $V_{\rm int}(r)-rV_c(r)$. Furthermore, in the RDW matrix elements for the cross sections, the distorted waves of the incident and final channels were calculated in the field of the static potential of the respective channels. This is in contrast to the usual distorted-wave procedure of using the static potential of the final state in both channels. The cross sections from both the frozen-core and multiconfiguration models are very similar in shape, with the frozen-core results being very slightly larger and only barely distinguishable from the corresponding multiconfiguration results on a typical graph. Consequently, for reasons of clarity, only the cross sections from the multiconfiguration model are presented in Fig. 3 below.

B. RCCC calculations

The RCCC method was recently described by Fursa and Bray [16], in connection with its application to e-Cs collisions. For the present work, we followed the same computational scheme for the calculation of e-Au scattering. The gold atoms were described by a model of one active electron above an inert (Xe $4f^{14}5d^{10}$) Dirac-Fock core. The set of gold atom wave functions was obtained by diagonalizing the Dirac Hamiltonian for the active valence electron in a Sturmian basis of Dirac L spinors [17]. The result of the diagonalization is a set of square-integrable states that correspond to the discrete spectrum of the target and also provide a discretization of the target continuum. Adding a one-electron polarization potential allowed us to obtain an accurate fit to the low-lying discrete energy levels of gold. Furthermore, the square-integrable discretization of the target continuum enabled us to systematically study the effect of coupling to ionization channels on the calculated bound-state excitation cross sections. This was done by increasing the number of states included in the e-Au scattering expansions. The latter calculations were performed by generating a multichannel close-coupling expansion of the total (electron plus target atom) wave function. This multichannel expansion of the total wave function was substituted into the total Dirac-Coulomb Hamiltonian of the scattering system and converted to a set of Lippmann-Schwinger equations for the T-matrix elements. Upon solution of the Lippmann-Schwinger equations [16], we obtained a set of scattering amplitudes and cross sections for the transitions of interest.

We emphasize that the quasi-one-electron model described above is a rather crude approximation to the actual atomic structure of gold. The major problem is related to the opening of the $5d^{10}$ core. The importance of this effect is clearly seen from the fact that the first excited states of gold are actually of the $5d^9 6s^2$ configuration. Although we can obtain an accurate fit to the energy levels for the $(\ldots 5d^{10}nl)$ part of the spectrum, this does not guarantee the accuracy of the underlying wave functions. As mentioned above, a noteworthy example is the optical oscillator strength for the $(5d^{10}6s)^2S_{1/2}\rightarrow(5d^{10}6p)^2P_{1/2,3/2}$ resonance transitions. In our model, we obtained values of 0.366 $(P_{1/2})$ and 0.771 $(P_{3/2})$ in the length form of the electric dipole operator. These numbers are nearly a factor of 2 larger than the recommended values [6] of 0.176 $(P_{1/2})$ and 0.351 $(P_{3/2})$, respectively.

The most consistent way to address this problem is to include configurations corresponding to the opening of the $5d^{10}$ core (see the next section). However, the resulting target wave functions are very complex and difficult to use in large-scale collision calculations. In the present RCCC calculations, therefore, we adopted a much simpler approach, which specifically addressed the problem of the otherwise incorrect optical oscillator strengths for the two resonance transitions in gold; namely, we added a two-electron polarization potential, which modified the projectile-target electron-electron Coulomb potential. Note that we previously used such a potential successfully to treat electron scattering from alkali-earth-metal atoms [18]. In the present case, this polarization potential did not change the target structure, but it did affect, significantly, the results for the quasi-two-electron problem of e-Au scattering. In particular, one can show that the generalized optical oscillator strength for the resonance transition calculated in the Born approximation in the limit of small momentum transfer will converge to the value of the optical oscillator strength calculated with the correspondingly modified formula for the dipole operator [19]. The values of the optical oscillator strength obtained in our so modified calculations were 0.160 $(P_{1/2})$ and 0.373 $(P_{3/2})$, i.e., within 10% of the recommended values. With the addition of the two-electron polarization potential, we could guarantee the correct high-energy behavior of the cross sections for the resonance transitions in gold with sufficient accuracy (at least for the present study), as well as consistency with the experimental normalization.

We performed calculations of the e-Au scattering in a number of close-coupling models including 3, 9, 19, 33, 64, and 90 states. All of these shared the same structure description for the three discrete states of interest. Since the models only differed in the number of states included in the close-coupling expansion, we could conduct some convergence

studies. The underlying Au structure model was generated by diagonalizing the target Hamiltonian in a Dirac L-spinor basis containing 54 functions with exponential cutoffs α=4.2, 3.6, 2.8, and 2.9 for the $S_{1/2}$, $P_{1/2,3/2}$, $D_{3/2,5/2}$, and $F_{5/2,7/2}$ target symmetries, respectively. This diagonalization produced a maximum of 19 states in the discrete spectrum. The differences between the three-, nine-, and 19-state results then indicate the importance of including additional target bound states in the close-coupling expansion, while comparison with results from models with progressively larger numbers of continuum pseudostates assesses the importance of coupling to ionization channels.

The RCCC results presented in the next section are a combination of those obtained in the various models mentioned above, using the minimum number of states in the close-coupling expansion that practically produced converged results. Finally, the Born subtraction technique was employed to achieve convergence in the partial-wave contribution to the calculated cross sections.

C. DBSR calculations

The Dirac B-spline R-matrix (close-coupling) approach is a newly developed extension of the BSR complex [20] to the fully relativistic Dirac scheme. It is described in detail in a recent application to e-Cs collisions [21]. The distinguishing features of the method are (i) the ability to use term-dependent, and hence nonorthogonal, sets of one-electron orbitals (Dirac spinors in the present case) in the target description and (ii) B splines as the underlying, effectively complete basis to expand the wave function of the projectile. Furthermore, it is an all-electron approach, and hence core-valence correlation effects (such as the core polarization) can be described *ab initio*. As usual, the R-matrix method allows for an efficient calculation of results for a large number of collision energies, as needed particularly in near-threshold regimes that are often dominated by resonance structures. On the other hand, using a basis expansion for the projectile wave function limits the energy range to low and intermediate energies. In addition, the number of states that can be included in the close-coupling expansion is currently less than in the RCCC approach, and it is particularly difficult to include a sufficient number of pseudostates to account for coupling to the ionization continuum.

As mentioned previously, the low-energy spectrum of the gold atom consists of states with configurations $(5d^{10}nl)^2L$, as well as core-excited states with configurations $(5d^9 6s^2)$ and $(5d^9 6s 6p)$, respectively. For the first set, the principal correlation effects originate from the interaction of the valence electron with the core, whereas for the core-excited states the valence correlation itself is also important. Both these correlation corrections were included *ab initio* by using extensive multiconfiguration expansions for the target wave functions, including many configurations with an excited core. These calculations were carried out in the Dirac-Fock approximation using the GRASP2K relativistic atomic structure package [22]. Note that we employed relaxed $5d$, $6s$, and $6p$ one-electron orbitals for the core-excited states. These orbitals are not orthogonal to the corresponding orbitals in the $(5d^{10}nl)$ states. In order to make the subsequent collision calculation manageable, we restricted our target expansions to configurations with mixing coefficients greater than 0.005. The resulting target excitation energies agreed with the experimental values at the level of 0.1 eV or better, including the $(5d^9 6s^2)^2 D_{5/2,3/2}$ states. The oscillator strengths for the $6s \rightarrow 6p_{1/2}$ and $6s \rightarrow 6p_{3/2}$ transitions were obtained as 0.172 and 0.376, respectively, in close agreement with the experimental values 0.176 and 0.351 [6].

In the present calculations, we used the Dirac-Coulomb Hamiltonian to describe both the N-electron target and the $(N+1)$-electron collision systems. The total wave function for each partial-wave symmetry was constructed from four-component Dirac spinors. Note that the radial functions for the large and small components were expanded in separate B-spline bases of different order. This allowed us to avoid the occurrence of pseudostates. We used a semiexponential grid for the B-spline knot sequence and a relatively large number (150) of splines to cover the inner region up to the R-matrix radius of $30a_0$. This large number of splines was required to correctly describe the finite-size nuclear model with a Fermi potential adopted in the present work.

The DBSR close-coupling expansion contained ten target states with configurations $(5d^{10}6s,\ 6p,\ 7s,\ 7p,\ 6d)$ and $(5d^9 6s^2)$. In order to check the convergence, we also carried out 15-state calculations, where five additional states with configurations $(5d^9 6s 6p)$ were included. We calculated partial-wave contributions up to J=50 numerically and used a geometric extrapolation scheme to account for even higher partial waves if necessary. The cross sections, and any other scattering parameters of interest, were then calculated in the same way as in the standard R-matrix approach.

IV. RESULTS AND DISCUSSION

Figure 3 exhibits the individual integral cross sections for electron-impact excitation of the $(5d^{10}6p)^2P_{1/2}$ and $(5d^{10}6p)^2P_{3/2}$ states in gold as well as the ratio $\sigma(^2P_{3/2})/\sigma(^2P_{1/2})$. The experimental data are compared with results obtained with the RDW, RCCC, and DBSR models described in the text. We note overall good agreement between experiment and the various theoretical predictions. Even the first-order plane-wave Born approximation (FBA), calculated with the target descriptions used in the RCCC model, does quite well, with the typical problem of overestimating the cross section near the maximum. For energies of 20 eV and higher, the RDW (without cascade) and the DBSR (with cascade) results are very similar. The RCCC results, on the other hand, are generally lower than those from the other models. Looking at the RCCC with and without cascades suggests a maximum cascade contribution of about 10% near 20 eV. A similar size of the cascade effect was seen in the corresponding DBSR results (not shown). In addition, however, the DBSR method allows for an estimate of the cascade *loss* in the observed photon signal to the ground state due to transitions to the $(5d^9 6s^2)^2 D_{5/2,3/2}$ levels. Interestingly, this effect is significantly bigger for the $(5d^{10}6p)^2P_{3/2}$ state (about 7%) than for the $(5d^{10}6p)^2P_{1/2}$ state (about 1%).

Based on the similarity of the RDW and DBSR results, one might conclude that channel-coupling and cascade ef-

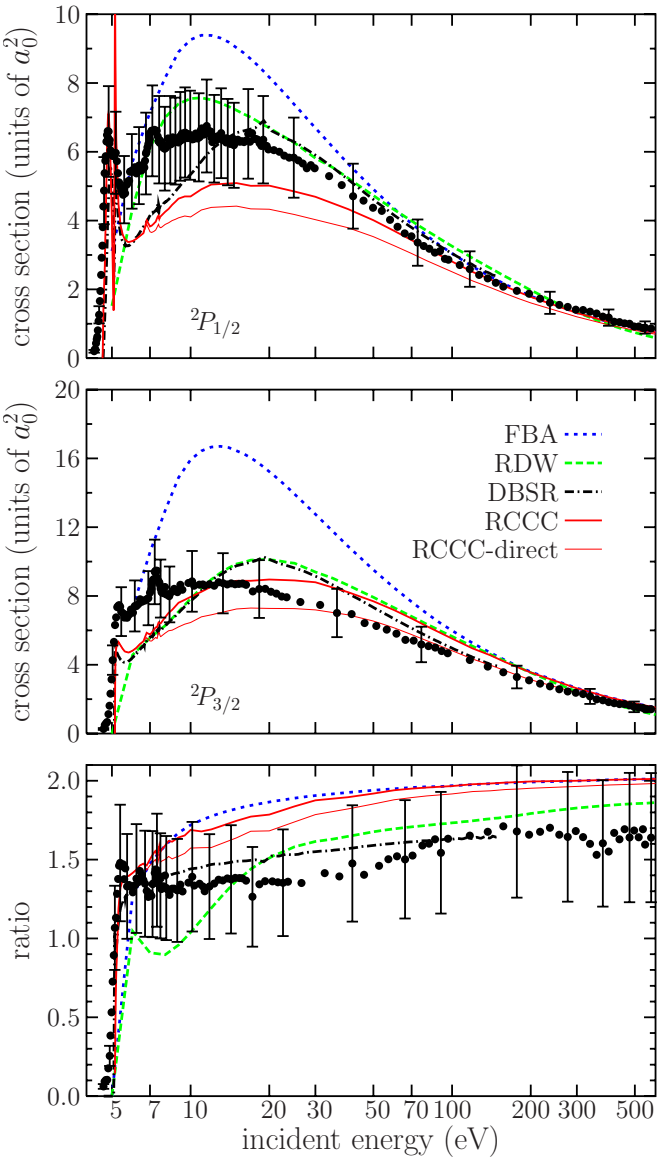

FIG. 3. (Color online) Cross sections and ratio for electron-impact excitation of the $(5d^{10}6p)^2P_{1/2}$ and $(5d^{10}6p)^2P_{3/2}$ states in gold. The present experimental data are compared with results obtained with the RDW, RCCC, and DBSR models described in the text. The curves labeled "RDW" and "RCCC-direct" show the direct cross sections, whereas all the other curves include cascade effects. Also shown are the results from a first-order plane-wave Born approximation (FBA) calculated with the target descriptions used in the RCCC model. If cascade effects are neglected, the nonrelativistic value for the ratio $\sigma(^2P_{3/2})/\sigma(^2P_{1/2})$ is 2.0.

fects become essentially negligible for energies above 30 eV. More accurately, however, the increase of the DBSR predictions due to cascades (except for the near-threshold region where the loss to the ^2D states dominates) is accidentally comparable to the reduction of the signal due to the inclusion of channel coupling when compared to the RDW results. Furthermore, the lower RCCC results near the peak indicate a potential importance of coupling to the continuum, which is only accounted for to a limited extent in the current DBSR model. Test calculations with a different number of states

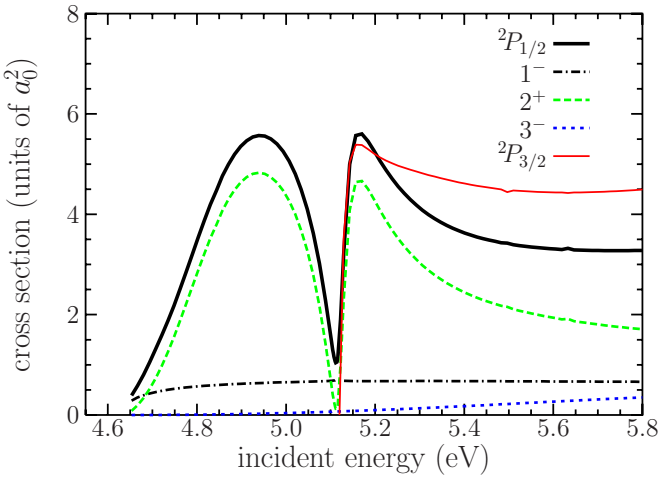

FIG. 4. (Color online) DBSR cross section for excitation of the $(5d^{10}6p)^2P_{1/2,3/2}$ states in the near-threshold regime, as well as the three largest J^π partial-wave contributions to the excitation of the $(5d^{10}6p)^2P_{1/2}$ state.

included in the RCCC model indeed yielded larger values of the cross-section maximum. Unfortunately, the experimental uncertainties of only 20% are still too large to clearly favor one model over the others. These were challenging experiments, so that a significant reduction in this error is unlikely. Of course, neither the FBA nor RDW is expected to work well in the near-threshold regime.

Regarding the ratio $\sigma(^2P_{3/2})/\sigma(^2P_{1/2})$, the DBSR and RDW predictions differ significantly from the nonrelativistic value of 2.0 (if cascades are neglected as well) even at high energies (see Fig. 3). The target description used in the RCCC model is such that (fortuitously) the nonrelativistic value seems to be approached closely. The experimental result also remains significantly below 2.0 at all energies, albeit with an uncertainty that encompasses essentially all the theoretical predictions. Using the experimental oscillator strengths and excitation energies in Eq. (1), one would expect the ratio to approach 1.8 for high energies.

Finally, Fig. 4 exhibits the DBSR results in the near-threshold regime. We show the cross sections for both fine-structure states, as well as the three largest partial-wave contributions to the excitation of the $(5d^{10}6p)^2P_{1/2}$ state. Not surprisingly, these are coming from the symmetries with total electronic angular momenta and parity (J^π) 1^-, 2^+, and 3^-. In a nonrelativistic framework, these correspond to incident partial waves with orbital angular momenta $l=1,2,3$. We also see that the double peak in the excitation cross section of the $(5d^{10}6p)^2P_{1/2}$ state is entirely due to the 2^+ symmetry. Further analysis shows that the contribution comes from the projectile having an initial orbital angular momentum $l_i=2$ and a final orbital angular momentum $l_f=1$. The structure also appears in the elastic channel for $l_i=2=l_f=2$ (not shown). Hence, this suggests a nonrelativistic classification of $(5d^{10}6p^2)^1D_2$ for the feature. In the relativistic framework, however, the structure is split and occurs close to both the $(5d^{10}6p)^2P_{1/2}$ and $(5d^{10}6p)^2P_{3/2}$ thresholds. The RCCC calculations (not shown) produce similar results to those of the DBSR regarding the position and the origin (2^+ symmetry)

of the double peak in the excitation cross section of the $(5d^{10}6p)^2P_{1/2}$ state in the near-threshold region. Both the DBSR and RCCC predictions are in qualitative agreement with the experimental findings.

V. CONCLUSIONS

In conclusion, we have presented experimental and theoretical results for integral cross sections for electron impact excitation of the $(5d^{10}6p)^2P_{1/2,3/2}$ levels in gold. Typically quite good agreement was found between each of the relativistic methods (RDW, RCCC, and DBSR) and the measured data, with the importance of incorporating relativistic effects for such a heavy target being demonstrated in this study. Even for this optically allowed transition, channel coupling to the continuum might be important as well. More theoretical work, in particular larger DBSR calculations going significantly beyond our currently available computational resources, would be desirable to draw more definite conclusions regarding this matter. Finally, near-threshold structures observed in the experimental measurements were also partially elucidated in our investigation. In particular, a strong resonance feature in the near-threshold excitation of the $(5d^{10}6p)^2P_{1/2}$ level was classified as being a $(5d^{10}6p^2)^1D_2$ temporary state of the negative gold ion.

ACKNOWLEDGMENTS

This work was supported, in part, by the Australian Research Council and by the United States National Science Foundation. We thank Dr. Laurence Campbell for his assistance in the production of this paper.

[1] L. C. Popovic, M. S. Dimitrijevic, and D. Tankosic, Astron. Astrophys. Suppl. Ser. **139**, 617 (1999).
[2] V. V. Chvykov, T. P. Kraposhina, S. N. Mazurov, T. P. Zaharova, and K. I. Zemskov, in *Pulsed Metal Vapour Lasers*, edited by C. E. Little and N. V. Sabotinov (Kluwer Academic, Dordrecht, 1996), p. 403.
[3] V. Zeman, R. P. McEachran, and A. D. Stauffer, Can. J. Phys. **74**, 889 (1996).
[4] S. Holst, W. Legler, R. Newjoto, and J. Pelis, J. Phys. B **23**, 2977 (1990).
[5] B. H. Bransden and C. J. Joachain, *Physics of Atoms and Molecules* (Longman, London, 1983).
[6] P. Hannaford, P. L. Larkins, and R. M. Lowe, J. Phys. B **14**, 2321 (1981).
[7] J. Migdalek and M. Garmulewicz, J. Phys. B **33**, 1735 (2000).
[8] Y.-K. Kim, Phys. Rev. A **64**, 032713 (2001).
[9] V. Zeman, R. P. McEachran, and A. D. Stauffer, J. Phys. B **27**, 3175 (1994).
[10] I. P. Grant, B. J. McKenzie, P. H. Norrington, D. F. Mayers, and N. C. Pyper, Comput. Phys. Commun. **21**, 207 (1980).
[11] I. B. Bersuker, Opt. Spectrosc. **3**, 97 (1957).
[12] S. Hameed, A. Herzenberg, and M. G. James, J. Phys. B **1**, 822 (1968).
[13] J. Migdalek and Y.-K. Kim, J. Phys. B **31**, 1947 (1998).
[14] J. Migdalek and W. E. Baylis, J. Quant. Spectrosc. Radiat. Transf. **22**, 1979 (1979).
[15] L. C. Owono Owono, M. G. Kwato Njock, and M. L. C. Owono Angue, Phys. Lett. A **339**, 343 (2005).
[16] D. V. Fursa and I. Bray, Phys. Rev. Lett. **100**, 113201 (2008).
[17] I. P. Grant and H. M. Quiney, Phys. Rev. A **62**, 022508 (2000).
[18] D. V. Fursa and I. Bray, J. Phys. B **30**, 5895 (1997).
[19] T. C. Caves and A. Dalgarno, J. Quant. Spectrosc. Radiat. Transf. **12**, 1539 (1972).
[20] O. Zatsarinny, Comput. Phys. Commun. **174**, 273 (2006).
[21] O. Zatsarinny and K. Bartschat, Phys. Rev. A **77**, 062701 (2008).
[22] P. Jönsson, X. He, C. Froese Fischer, and I. P. Grant, Comput. Phys. Commun. **177**, 597 (2007).